

Solar Wind Driven from GONG Magnetograms in the Last Solar Cycle

ZHENGUANG HUANG,¹ GÁBOR TÓTH,¹ NISHTHA SACHDEVA,¹ AND BART VAN DER HOLST¹

¹*Climate and Space Sciences and Engineering, University of Michigan, Ann Arbor, MI 48109, USA*

ABSTRACT

In a previous study, [Huang et al. \(2023\)](#) used the Alfvén Wave Solar atmosphere Model (AWSoM), one of the widely used solar wind models in the community, driven by ADAPT-GONG magnetograms to simulate the solar wind in the last solar cycle and found that the optimal Poynting flux parameter can be estimated from either the open field area or the average unsigned radial component of the magnetic field in the open field regions. It was also found that the average energy deposition rate (Poynting flux) in the open field regions is approximately constant. In the current study, we expand the previous work by using GONG magnetograms to simulate the solar wind for the same Carrington rotations and determine if the results are similar to the ones obtained with ADAPT-GONG magnetograms. Our results indicate that similar correlations can be obtained from the GONG maps. Moreover, we report that ADAPT-GONG magnetograms can consistently provide better comparisons with 1 AU solar wind observations than GONG magnetograms, based on the best simulations selected by the minimum of the average curve distance for the solar wind speed and density.

1. INTRODUCTION

Accurately predicting the solar wind distribution at various locations in the heliosphere is one of the major objectives in the solar and heliosphere community, as well as the space weather community. The background solar wind plays a crucial role in determining the strength and arrival time of various drivers of space weather events, e.g., Coronal Mass Ejections (CMEs), Solar Energetic Particles (SEPs) and co-rotating interaction regions (CIRs). CIRs or CMEs can cause large geomagnetic disturbances (geomagnetic storms) that threaten advanced technology that we are highly reliant on. For example, the 1989 geomagnetic storm caused a widespread effect on the power grid system including a blackout of the Hydro-Québec system (Boteler 2019).

There are many different solar wind models in the community, from empirical or semi-empirical models like the commonly used Wang-Sheeley-Argé (WSA) model (Wang & Sheeley 1990, 1992; Arge & Pizzo 2000), to first principles models focusing on small scale reconnections (Axford & McKenzie 1992; Fisk et al. 1999; Fisk & Schwadron 2001; Schwadron & McComas 2003; Fisk 2003; Yamauchi et al. 2004) as well as plasma wave heating (Tu & Marsch 1997; Mikić et al. 1999; Hu et al. 2000; Usmanov et al. 2000; Dmitruk et al. 2002; Markovskii & Hollweg 2002; Li & Habbal 2003; Vásquez et al. 2003; Suzuki & Inutsuka 2005; Cohen et al. 2007; Cranmer 2010; Feng et al. 2011; Verdini et al. 2010; Osman et al. 2011; Chandran et al. 2011; Lionello et al. 2014), and the newly developed machine learning model by Upendran et al. (2020). All these models make different assumptions, and/or apply different methods to predict the solar wind. But there is (at least) one thing in common: all of them need observational input(s) from the Sun, either the observed magnetic field on the surface, or the solar corona ultraviolet image(s).

The photospheric magnetic field is the primarily used observational input for solar wind models. There are two major types of observational products: synoptic magnetograms, which reconstruct the map from 27-day of magnetic field observations with some simple weighting factors (e.g., the Global Oscillation Network Group (GONG, Harvey et al. 1996) uses \cos^4 of longitude) to ensure measurements taken at a particular time contribute most to that Carrington longitude in the synoptic map; and synchronic magnetograms, which take the photospheric magnetic field observations and apply surface flux transport models to simulate the evolution of the surface magnetic field while

assimilating new observations. There are different observational sources used in both types of magnetograms, e.g., the Helioseismic Magnetic Imager (HMI, [Schou et al. 2012](#)) on the Solar Dynamics Observatory (SDO), the Michelson Doppler Imager (MDI, [Scherrer et al. 1995](#)) on the Solar and Heliospheric Observatory (SoHO), the GONG, the Mt. Wilson Observatory (MWO, [Ulrich et al. 2002](#)), the Synoptic Optical Long-term Investigations of the Sun (SOLIS, [Keller et al. 2003](#)) at the National Solar Observatory (NSO), and the Wilcox Solar Observatory (WSO, [Babcock 1953](#); [Scherrer et al. 1977](#)). Also, there are different flux transport models, e.g., the Air Force Data Assimilative Photospheric flux Transport (ADAPT, [Hickmann et al. \(2015\)](#)), the Advective Flux Transport (AFT, [Upton & Hathaway \(2014b,a\)](#)), and the Lockheed Martin flux transport model ([Schrijver & De Rosa 2003](#)).

The input magnetogram has a strong impact on the simulated solar wind. [Gressl et al. \(2014\)](#) used four different magnetograms (MDI, NSO, MWO and GONG) to simulate the solar wind and showed that the choice of the synoptic map for the solar wind models significantly affects the model performance. [Jian et al. \(2015\)](#) compared multiple coronal and heliospheric models and different magnetograms and arrived at similar conclusions. Recently, [Sachdeva et al. \(2019\)](#) used the Alfvén Wave Solar atmosphere Model (AWSoM) to simulate solar minimum conditions and they noticed that the simulated solar wind based on the ADAPT-GONG magnetogram agrees better with observations, than the GONG magnetogram when all other model parameters are kept the same. [Jin et al. \(2022\)](#) assessed the influence of input magnetic maps on modeling the solar wind and concluded that it is important to consider the model uncertainty due to the imperfect magnetic field measurements. [Sachdeva et al. \(2021\)](#); [Sachdeva et al. \(2023\)](#) used AWSoM to simulate solar maximum conditions with different input magnetograms, and confirmed that the simulated solar wind at 1 AU can be very different when different input magnetograms are used.

In this study, we will expand our previous work ([Huang et al. \(2023\)](#), Paper I, hereafter) by simulating the solar wind using GONG magnetograms, for the same Carrington rotations that Paper I studied using ADAPT-GONG magnetograms. We then investigate how GONG maps affect the simulated solar wind at 1 AU during different phases of the last solar cycle. Both ADAPT-GONG and GONG

magnetograms are widely used as the input magnetic field map for solar wind modeling. They take the same observations but construct the maps using different techniques. ADAPT-GONG applies the ADAPT surface flux transport model while GONG takes simple weighting factors. Systematically evaluating the model performance when driven by the two different maps can provide insights if a particular type of map provides better simulated solar wind, which is critical for real-time solar wind prediction. We will use AWSoM (Sokolov et al. 2013; van der Holst et al. 2014; Sokolov et al. 2021) to simulate the steady-state background solar wind. AWSoM is one of the widely used solar wind models in the community. It is open-source on GitHub (<https://github.com/MSTEM-QUDA/SWMF>) and can also be accessed via the runs-on-request service provided by the Community Coordinated Modeling Center (CCMC). AWSoM has been extensively validated with in-situ and remote observations under different solar wind conditions (Jin et al. 2012; Oran et al. 2013; Sachdeva et al. 2021; Huang et al. 2023; Szente et al. 2022, 2023), as well as at different heliocentric distances including Parker Solar Probe locations (van der Holst et al. 2019, 2022).

2. METHODOLOGY

AWSoM is implemented in the BATS-R-US (Block Adaptive Tree Solar Wind Roe-type Upwind Scheme) code (Groth et al. 2000; Powell et al. 1999) within the Space Weather Modeling Framework (SWMF) (Tóth et al. 2005, 2012; Gombosi et al. 2021). The main input of the model is the observed radial component of the photospheric magnetic field, a magnetogram, at the inner boundary. The density and temperature at the inner boundary are uniformly specified as $n = 2 \times 10^{17} \text{ m}^{-3}$ and $T = 50,000 \text{ K}$. AWSoM assumes that the pressure gradient and the nonlinear dissipation of the Alfvén wave turbulence are the only sources for accelerating and heating the solar wind, respectively. At the outer boundary, AWSoM applies a zero gradient condition allowing the super-fast magnetosonic solar wind to freely leave the domain. In depth discussions of the physics can be found in Sokolov et al. (2013); van der Holst et al. (2014, 2022).

Significant progress has been made in understanding how the input parameters of AWSoM affect the simulation results recently. Jivani et al. (2023) used uncertainty quantification to study the effect of using different model parameters and determined the three major parameters impacting the

simulated output. These are the Poynting flux parameter, associated with the energy input at the inner boundary for heating the corona and driving the solar wind; the perpendicular correlation length parameter, associated with how solar wind plasma gains energy from the Alfvén wave turbulence in the simulation domain; and the multiplicative factor for the input magnetogram, which is related to the uncertainty of the magnetic field observations. Paper I focused on the variation of the optimal value for the Poynting flux parameter in the last solar cycle and determined that it is linearly correlated with the area of the open field regions and anti-correlated with the average unsigned radial component of the magnetic field.

In this study, we apply the same approach as Paper I. We simulate the same Carrington rotations as Paper I, which are listed in Table 1, so that we can have a direct comparison between simulation results using the ADAPT-GONG and GONG maps. The ADAPT-GONG magnetograms are available at <https://gong.nso.edu/adapt/maps/gong>, and the GONG magnetograms can be accessed on <https://gong.nso.edu/data/magmap/>. We apply a similar approach as in Paper I and vary the the Poynting flux parameter between 0.3 and $1.2 \text{ MWm}^{-2}\text{T}^{-1}$ with every $0.05 \text{ MWm}^{-2}\text{T}^{-1}$, except for two rotations, CR2137 and CR2198, in which the optimal values are outside the typical range. For CR2137, the range is extended below $0.3 \text{ MWm}^{-2}\text{T}^{-1}$ by adding extra points as $[0.1, 0.125, 0.15, 0.175, 0.2, 0.25] \text{ MWm}^{-2}\text{T}^{-1}$; and for CR2198, three extra points of $[1.25, 1.3, 1.35] \text{ MWm}^{-2}\text{T}^{-1}$ are included. All other parameters are set with the default values. To be specific, the perpendicular correlation length parameter is set to $1.5 \times 10^5 \text{ m T}^{\frac{1}{2}}$. For the GONG magnetograms, we apply a scaling factor of 3.75 to account for the uncertainty of the synoptic magnetogram observations, especially the very weak field in high latitude regions. To be specific, we set the radial component of the magnetic field (B_r) to $\text{sign}(B_{r\text{GONG}}) \cdot \min(3.75 \cdot |B_{r\text{GONG}}|, 5 + |B_{r\text{GONG}}|)$, where $B_{r\text{GONG}}$ is the observed B_r from the GONG magnetogram and the unit is in Gauss. This setting is consistent with previous studies (Cohen et al. 2007; Jin et al. 2012). Riley (2007) also applies a similar factor to study the open flux problem. As Hickmann et al. (2015) applied their scaling factor to derive the ADAPT-GONG magnetogram, we do not apply such a multiplicative factor for ADAPT-GONG magnetograms. There are 180 simulations in total in this study. Each simulation takes about 4000

Carrington Rotation	UTC Time of the Maps	
	ADAPT-GONG	GONG
2106	2011-2-2 02:00	2011-2-1 23:54
2123	2012-5-16 20:00	2012-5-16 17:54
2137	2013-5-28 20:00	2013-5-28 20:04
2154	2014-9-2 20:00	2014-9-2 20:04
2167	2015-8-23 02:00	2015-8-23 02:04
2174	2016-3-3 02:00	2016-3-3 02:14
2198	2017-12-17 02:00	2017-12-17 02:04
2209	2018-10-13 06:00	2018-10-13 06:04
2222	2019-10-2 02:00	2019-10-2 02:14

Table 1. All the ADAPT-GONG and GONG magnetograms used in this study. For all the ADAPT-GONG maps, the 7th realization is picked as mentioned in Paper I.

to 5000 CPU hours (1120 cores running for about 3.5-4.5 hours) for the Intel 8280 “Cascade Lake” type CPU, leading to a total cost of about 800K CPU hours.

We use the curve distance, introduced by [Sachdeva et al. \(2019\)](#), between the simulation output and in situ observations at 1 AU to quantify the model performance. We select the optimal value of the Poynting flux parameter when the average of the curve distances of the solar wind density and velocity reaches its minimum, the same as Paper I.

3. SIMULATION RESULTS

For clear one-to-one comparisons between the current study and our previous results using ADAPT-GONG maps (Paper I), we show figures similar to Paper I. We plot the AWSoM simulated solar wind (driven by GONG synoptic maps) for the same Carrington rotations: CR2106 near solar minimum in Figure 1, and CR2137 near solar maximum in Figure 2. Because we only change the values of the Poynting flux parameter of AWSoM, this figure clearly demonstrates the variations in the simulated solar wind results at 1 AU due to the different Poynting flux parameters. Similar to Figure 1 in Paper I, the simulations with different Poynting flux parameters are shown in blue and the optimal

value of the Poynting flux parameter is highlighted in red. These figures share some similarities: the variations of the solar wind due to different Poynting flux parameters are smaller near solar minimum (CR2106) and larger near solar maximum (CR2137); and some Poynting flux parameters produce unphysical results for a relatively active Sun (CR2137). But there are some distinct differences: the simulated solar wind bulk velocity based on the GONG magnetograms (Panels (a) in Figures 1 and 2) is significantly larger than the ADAPT-GONG magnetograms (Panels (b) in Figures 1 and 2), while the density is about the same or slightly smaller.

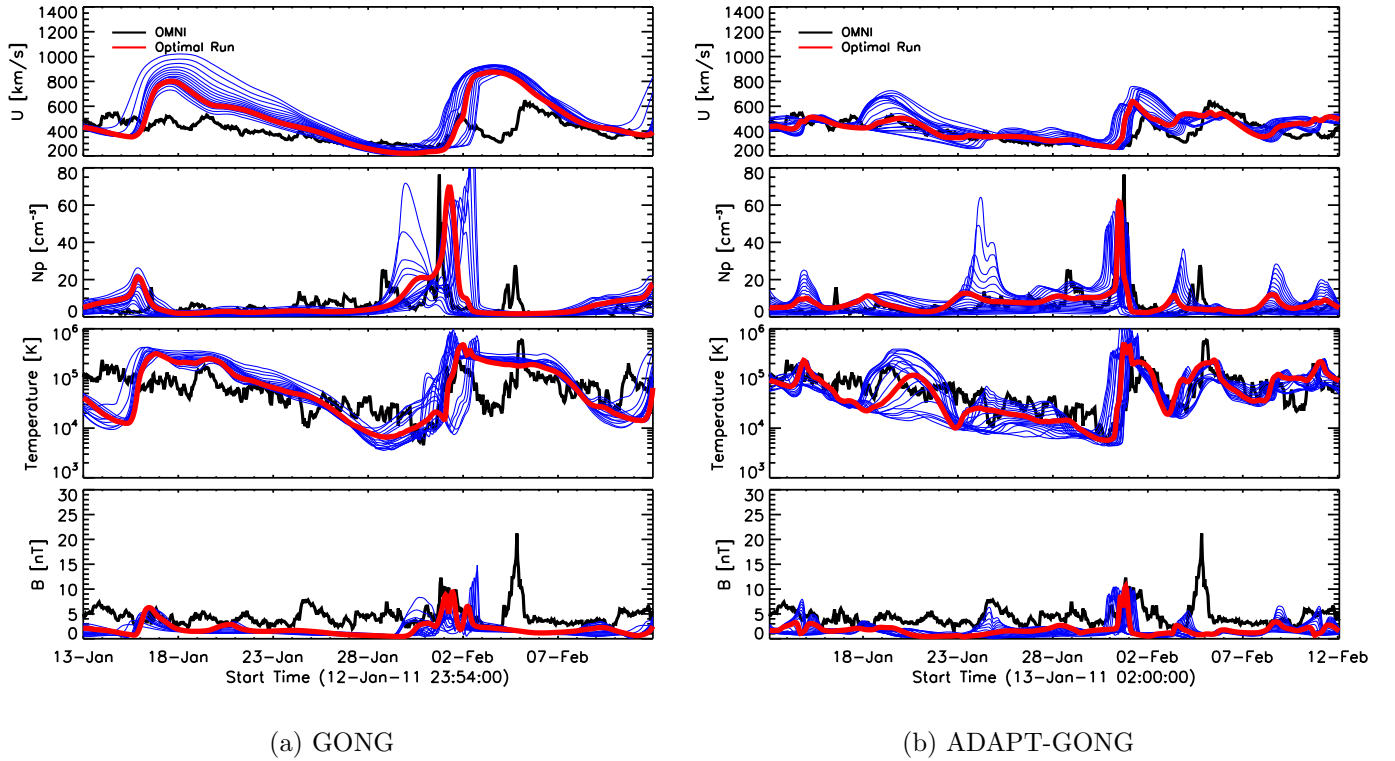


Figure 1. Comparison between the AWSoM simulated solar wind (blue and red lines) and the hourly OMNI data (black lines) at 1 AU, for CR2106, which is near solar minimum in 2011. Each blue line is associated with a specific value of the Poynting flux parameter, and the red line highlights the simulated solar wind using the optimal Poynting flux parameter. Panel (a) is based on the GONG magnetogram, while Panel (b) is a reproduction based on the ADAPT-GONG magnetogram for the same Carrington Rotation from Paper I.

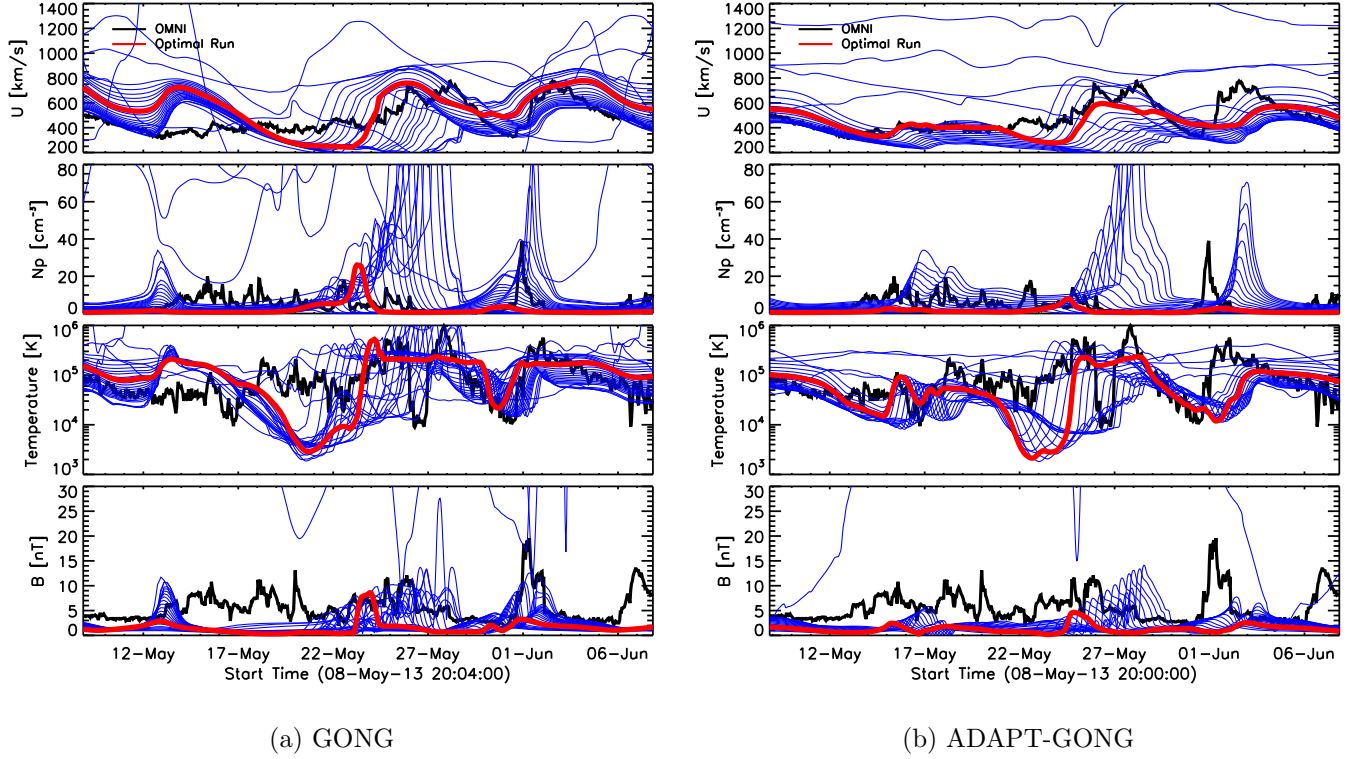


Figure 2. This figure shows a similar comparison as Figure 1 but for CR2137, which is near solar maximum in 2013. Panel (a) is based on the GONG magnetogram, while Panel (b) is a reproduction based on the ADAPT-GONG magnetogram from Paper I.

Paper I used the curve distance formula introduced by Sachdeva et al. (2019) to quantify the solar wind variations due to different Poynting flux parameters. We use the identical method in this study for a direct comparison. Figure 3 show the same quantities as Figure 2 in Paper I: the curve distance between the simulated solar wind density (top), bulk velocity (middle), and the average of the density and velocity distances (bottom) for the GONG magnetograms (in black) and ADAPT-GONG magnetograms (in blue), with the red and orange stars highlighting the local optimal Poynting flux parameter for the corresponding sub-figure. The optimal Poynting flux parameter is selected when the average of the density and velocity distances reaches its minimum, which is the same criteria as applied in Paper I. Similar features can be identified between GONG and ADAPT-GONG magnetograms. The simulated solar wind becomes unphysical when the Poynting flux parameter is larger than a certain value for a CR2137 (near solar maximum). The threshold is around $0.7 \text{ MWm}^2\text{T}^{-1}$ in this

study, slightly smaller than the $0.75 \text{ MWm}^2\text{T}^{-1}$ for the ADAPT-GONG magnetogram in Paper I. We also identify a monotonic increase of the distance when the Poynting flux parameter is smaller or larger than the local optimal value, except for the distance value plot for the solar wind bulk velocity for CR2106 in Panel (a). The curve distance for the solar wind bulk velocity for CR2106 is monotonically declining. It is unclear if it has reached its minimum yet. But because we select the optimal value based on the average of the velocity and density curve distances, the optimal value is already identified. To save computational cost, we do not extend the range of Poynting flux parameter for this rotation to confirm if the distance for the velocity will increase after it reaches its minimum. The monotonic trend is also identified in Paper I, which again suggests that the selection of the optimal value is reliable. Moreover, compared to the ADAPT-GONG results reproduced from Paper I, we notice larger curve distances when GONG magnetograms are used, which is consistent with the discussion above.

In order to better quantify the differences between the curve distances obtained from ADAPT-GONG and GONG magnetograms, we list the minimum values of the average distance of the solar wind density and bulk velocity in Table 2. We confirm that for most of the rotations in the study (8 out of 9), the optimal runs based on ADAPT-GONG magnetograms give smaller minimum distance values than the GONG magnetograms, with only one exception for CR2154 when the GONG magnetogram provides a slightly better result than the ADAPT-GONG magnetogram.

Next, following Paper I, we examine if the optimal Poynting flux parameter has any relation with the area of the open field regions and/or the average unsigned radial component of the magnetic field ($|B_r|$). The results are presented in Figure 4. We conclude that similar relations exist for simulations using GONG magnetograms as the one using ADAPT-GONG. However, the Spearman's correlation coefficients r for the GONG magnetograms are smaller than for the ADAPT-GONG magnetograms: the coefficient for the area of open field regions is 0.75, compared to 0.96 obtained with ADAPT-GONG magnetograms; and the coefficient for average unsigned $|B_r|$ in the open field regions is -0.79 , compared to -0.91 found with ADAPT-GONG magnetograms. Similarly, we obtain the following

formulas from the linear regression:

$$P = 0.42 \cdot A + 0.07 \pm 0.17 \quad (1)$$

$$P = -0.1 \cdot B + 1.57 \pm 0.21 \quad (2)$$

where P is optimal Poynting flux parameter in the unit of $[\text{MWm}^{-2}\text{T}^{-1}]$, A is the area of the open field regions in the unit of $[\text{R}_s^2]$, and B is the average unsigned B_r in the open field regions in the units of $[\text{G}]$. The standard error of the linear regression is given by the \pm terms. Compared to Equations 1 and 2 in Paper I, the slope for the open field area is the same while it is slightly a little larger for the average unsigned B_r in the open regions (-0.07 in Paper I). The intersections and standard errors for both equations are larger than the values in Paper I: the intersection/standard errors is $0.02/0.11$ for the open field area and $1.29/0.16$ for the average unsigned B_r in Paper I. The larger standard errors for GONG magnetograms result from larger variations when using different Poynting flux parameters as compared to ADAPT-GONG based simulations.

Paper I discovered that the average energy deposition rate (the Poynting flux) in the open field regions does not show significant variations among the simulated CRs. In order to further understand if this is true for the GONG magnetograms, we calculate the same quantity, which is shown in Figure 5. This figure is very similar to Figure 4 in Paper I. The average Poynting flux in the open field regions is found to be $52.5 \pm 14.26 \text{ Wm}^{-2}$, while it is $47.42 \pm 13.12 \text{ Wm}^{-2}$ for the ADAPT-GONG magnetograms in Paper I. They are essentially the same within the range of the standard error. To conclude, our study confirms that this behavior (small variations in the average deposition rate over time) is also valid when using the GONG magnetograms as the input for AWSoM.

4. SUMMARY AND DISCUSSIONS

We use the GONG magnetograms to simulate the background solar wind with AWSoM in the last solar cycle. We simulate the same Carrington rotations and follow the same methodology as described in Paper I. We only change the values of the Poynting flux parameter and use the default values for all other parameters. We also apply the same criteria in selecting the optimal Poynting flux parameter: the minimum value of the average of the curve distances between the simulated and

Carrington Rotation	Minimum Average Distance	
	ADAPT-GONG	GONG
2106	0.058	0.108
2123	0.095	0.113
2137	0.109	0.141
2154	0.117	0.092
2167	0.083	0.121
2174	0.184	0.193
2198	0.147	0.173
2209	0.115	0.147
2222	0.096	0.125

Table 2. The minimum average distances for ADAPT-GONG and GONG magnetograms.

observed density and the solar wind bulk velocity at 1 AU. This provides a direct comparison between simulations using ADAPT-GONG and GONG magnetograms, respectively.

There are several similarities between the results obtained from ADAPT-GONG magnetograms and GONG magnetograms. First of all, the optimal Poynting flux parameter is also linearly correlated with the open field area and anti-correlated with the average unsigned B_r in the open regions, even though the Spearman’s correlation coefficients are slightly less for GONG magnetogram: it drops from 0.96 to 0.75 for the open field area and drops from -0.91 to -0.79 for the average unsigned B_r in the open regions. Another similarity is that the average energy deposition rates from the two types magnetograms are almost the same. Performing a similar study with another first-principle solar wind model, such as the Magnetohydrodynamic Algorithm outside a Sphere (MAS, Mikić et al. (1999)) and the MHD model based on Reynolds-averaged solar wind equations (Usmanov et al. 2018), could help the community understand further if this conclusion holds for the Alfvén wave dissipation theory implemented into AWSoM, or this is generally true for other similar first-principle based solar wind models. Another direction to validate this finding is to derive the energy deposition rate in open field regions from observations during different phases of the solar cycle. There are some studies

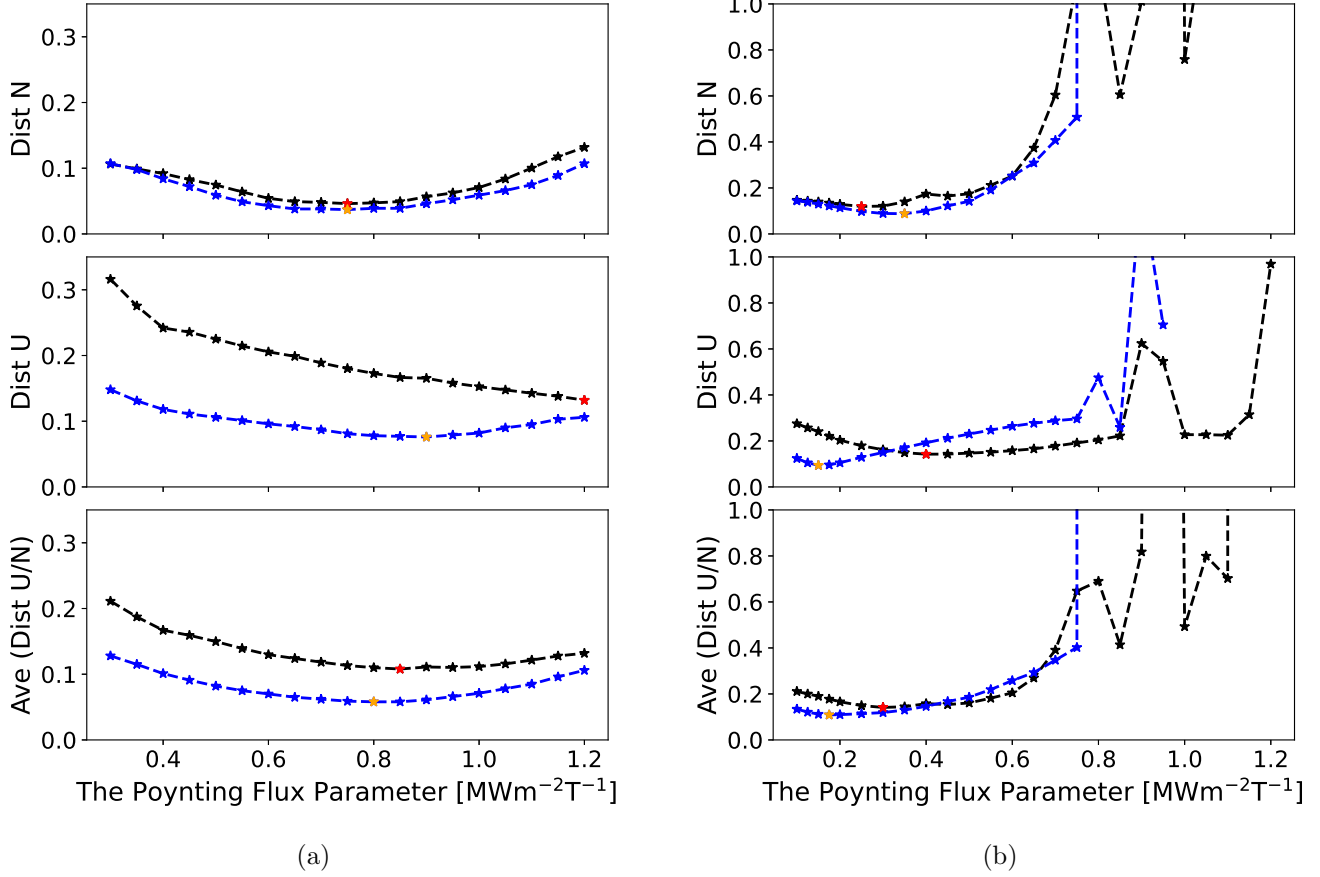


Figure 3. The variations of the distances as a function of different Poynting flux parameters. CR2106 is shown in Panel (a) while CR2137 is plotted in Panel (b). The relative curve distances for the solar wind density and velocity, as well as the average value of velocity and density distances are displayed from top to bottom, respectively. The black color is associated with the GONG magnetograms with the red star highlighting the optimal Poynting flux parameter value for the corresponding sub-figure, while the blue color is reproduced from Paper I for the ADAPT-GONG magnetogram results, with the yellow star highlighting the optimal Poynting flux parameter value.

along this direction. For example, [De Pontieu et al. \(2007\)](#) looked at the Alfvén wave energy at a specific period, while [Morton et al. \(2019\)](#) studied Alfvénic waves in a solar cycle without separating open and closed field regions.

We notice that simulated solar wind driven by the ADAPT-GONG magnetograms generally agrees better with OMNI data at 1 AU than the results driven by GONG magnetograms. For example, Figures 1 and 2 show that the simulated solar wind speed (from GONG magnetograms) is much

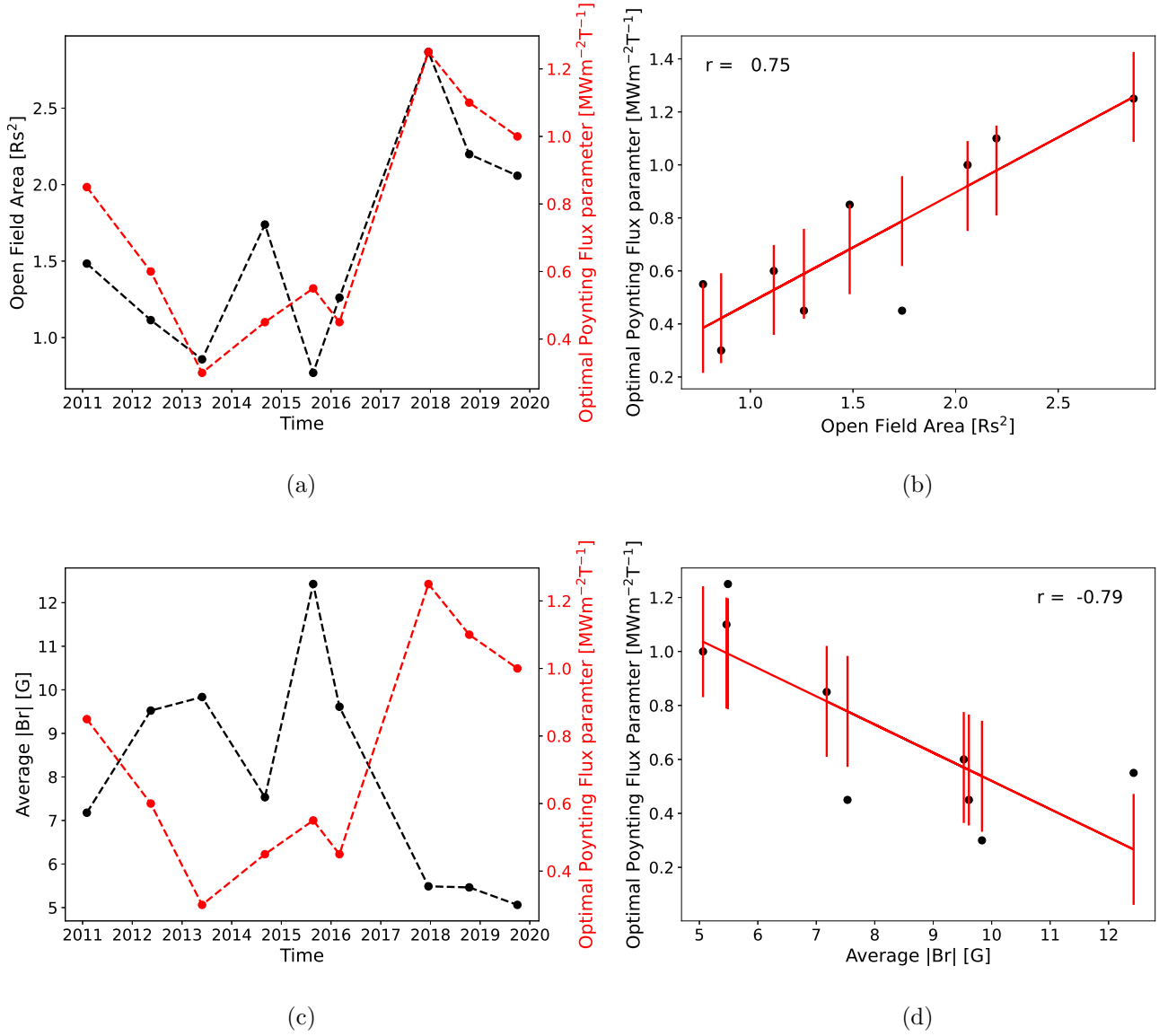


Figure 4. The correlations between the optimal Poynting flux parameter and the open field area as well as the average unsigned B_r in the open field regions. Panels (a) and (c) show the time evolution of the optimal Poynting flux parameter (in red), the open field area (in black) and the average unsigned B_r (in black). Panels (b) and (d) plot the linear regression results between the optimal Poynting flux parameter and the open field area and the average unsigned B_r , respectively, with the Spearman’s correlation shown in the upper left corner. The error bars indicate the standard deviation of the fit.

larger than the observed solar wind speed, as compared to Figure 1 in Paper I. This conclusion is confirmed by Table 2: the minimum distances from the ADAPT-GONG maps are smaller than the GONG maps, with only one exception for CR2154 in 2014, which is near solar maximum. This

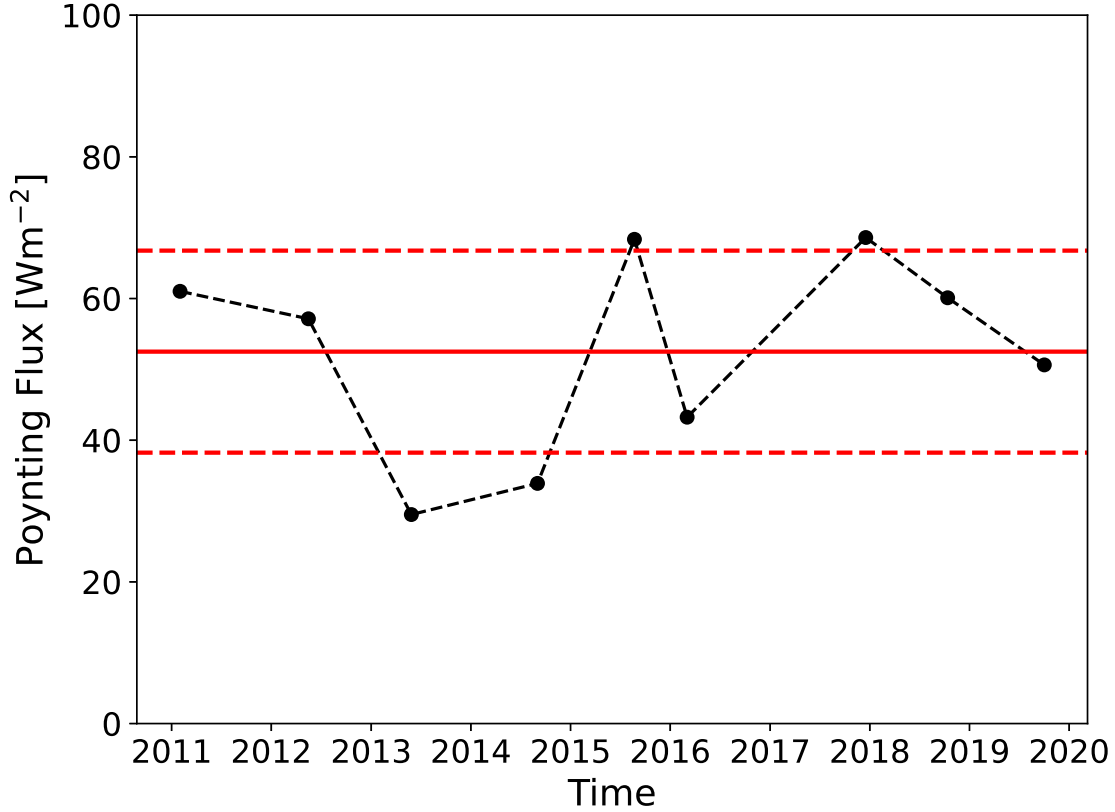


Figure 5. The time evolution of the average energy deposition rate (Poynting flux) in the open field regions between 2011 and 2019. The average value (52.5 Wm^{-2}) is shown with the horizontal red line while the standard deviation (14.3 Wm^{-2}) is plotted with the horizontal red dashed lines.

exception could be due to the more complicated flux transport process in a very active Sun than a relatively quiet Sun, and the ADAPT algorithm may be inaccurate in that scenario.

Our study is an important step in using a first-principle solar wind model for real-time solar wind prediction. Paper I and our results derived empirical formulas for the optimal Poynting flux parameter of AWSoM, and we show AWSoM can produce reasonable solar wind predictions at 1 AU, if the Poynting flux parameter is correctly set. Both Paper I and the current study cover only one Carrington rotation per year between 2011-2019. It is to be checked if the empirical formulas will hold if more rotations are included in the last solar cycle and/or other solar cycles are added. These questions will be addressed in future work.

This work was primarily supported by the NSF PRE-EVENTS grant No. 1663800, the NSF SWQU grant No. PHY-2027555, the NSF Solar Terrestrial grant No. 2323303, and the NASA grants Nos. 80NSSC22K0269, 80NSSC23K0450 and 80NSSC22K0892.

We acknowledge the high-performance computing support from Cheyenne (doi:10.5065/D6RX99HX) provided by NCAR's Computational and Information Systems Laboratory, sponsored by the NSF, and the computation time on Frontera (doi:10.1145/3311790.3396656) sponsored by NSF and the NASA supercomputing system Pleiades.

This work utilizes data produced collaboratively between AFRL/ADAPT and NSO/NISP.

REFERENCES

- Arge, C. N., & Pizzo, V. J. 2000, *J. Geophys. Res.*, 105, 10465
- Axford, W. I., & McKenzie, J. F. 1992, in *Solar Wind Seven Colloquium*, ed. E. Marsch & R. Schwenn, 1–5
- Babcock, H. W. 1953, *ApJ*, 118, 387
- Boteler, D. H. 2019, *Space Weather*, 17, 1427
- Chandran, B. D. G., Dennis, T. J., Quataert, E., & Bale, S. D. 2011, *ApJ*, 743, 197
- Cohen, O., Sokolov, I. V., Roussev, I. I., et al. 2007, *ApJL*, 654, L163
- Cranmer, S. R. 2010, *Astrophys. J.*, 710, 676
- De Pontieu, B., McIntosh, S. W., Carlsson, M., et al. 2007, *Science*, 318, 1574
- Dmitruk, P., Matthaeus, W. H., Milano, L. J., et al. 2002, *Astrophys J.*, 575, 571
- Feng, X., Zhang, S., Xiang, C., et al. 2011, *ApJ*, 734, 50
- Fisk, L. A. 2003, *Journal of Geophysical Research (Space Physics)*, 108, 1157
- Fisk, L. A., & Schwadron, N. A. 2001, *SSRv*, 97, 33
- Fisk, L. A., Schwadron, N. A., & Zurbuchen, T. H. 1999, *J. Geophys. Res.*, 104, 19765
- Gombosi, T. I., Chen, Y., Glocer, A., et al. 2021, *Journal of Space Weather and Space Climate*, 11, 42
- Gressl, C., Veronig, A. M., Temmer, M., et al. 2014, *SoPh*, 289, 1783
- Groth, C. P. T., De Zeeuw, D. L., Gombosi, T. I., & Powell, K. G. 2000, *J. Geophys. Res.*, 105, 25053
- Harvey, J. W., Hill, F., Hubbard, R. P., et al. 1996, *Science*, 272, 1284
- Hickmann, K. S., Godinez, H. C., Henney, C. J., & Arge, C. N. 2015, *SoPh*, 290, 1105
- Hu, Y. Q., Esser, R., & Habbal, S. R. 2000, *J. Geophys. Res.*, 105, 5093
- Huang, Z., Tóth, G., Sachdeva, N., et al. 2023, *ApJL*, 946, L47

- Jian, L. K., MacNeice, P. J., Taktakishvili, A., et al. 2015, *Space Weather*, 13, 316
- Jin, M., Nitta, N. V., & Cohen, C. M. S. 2022, *Space Weather*, 20, e2021SW002894
- Jin, M., Manchester, W. B., van der Holst, B., et al. 2012, *ApJ*, 745, 6
- Jivani, A., Sachdeva, N., Huang, Z., et al. 2023, *Space Weather*, 21, e2022SW003262
- Keller, C. U., Harvey, J. W., & Giampapa, M. S. 2003, in *Society of Photo-Optical Instrumentation Engineers (SPIE) Conference Series*, Vol. 4853, *Innovative Telescopes and Instrumentation for Solar Astrophysics*, ed. S. L. Keil & S. V. Avakyan, 194–204
- Li, X., & Habbal, S. R. 2003, *Astrophys J. Lett*, 598, L125
- Lionello, R., Velli, M., Downs, C., Linker, J. A., & Mikić, Z. 2014, *The Astrophysical Journal*, 796, 111
- Markovskii, S. A., & Hollweg, J. V. 2002, *Geophys. Res. Lett.*, 29, 1843
- Mikić, Z., Linker, J. A., Schnack, D. D., Lionello, R., & Tarditi, A. 1999, *Physics of Plasmas*, 6, 2217
- Morton, R. J., Weberg, M. J., & McLaughlin, J. A. 2019, *Nature Astronomy*, 3, 223
- Oran, R., van der Holst, B., Landi, E., et al. 2013, *ApJ*, 778, 176
- Osman, K. T., Matthaeus, W. H., Greco, A., & Servidio, S. 2011, *Astrophys. J. Lett.*, 727
- Powell, K. G., Roe, P. L., Linde, T. J., Gombosi, T. I., & de Zeeuw, D. L. 1999, *Journal of Computational Physics*, 154, 284
- Riley, P. 2007, *ApJL*, 667, L97
- Sachdeva, N., van der Holst, B., Manchester, W. B., et al. 2019, *ApJ*, 887, 83
- Sachdeva, N., T³th, G., Manchester, W. B., et al. 2021, *Earth and Space Science Open Archive*, 13
- Sachdeva, N., Manchester, Ward B., I., Sokolov, I., et al. 2023, *ApJ*, 952, 117
- Scherrer, P. H., Wilcox, J. M., Svalgaard, L., et al. 1977, *SoPh*, 54, 353
- Scherrer, P. H., Bogart, R. S., Bush, R. I., et al. 1995, *SoPh*, 162, 129
- Schou, J., Scherrer, P. H., Bush, R. I., et al. 2012, *SoPh*, 275, 229
- Schrijver, C. J., & De Rosa, M. L. 2003, *SoPh*, 212, 165
- Schwadron, N. A., & McComas, D. J. 2003, *ApJ*, 599, 1395
- Sokolov, I. V., van der Holst, B., Oran, R., et al. 2013, *ApJ*, 764, 23
- Sokolov, I. V., Holst, B. v. d., Manchester, W. B., et al. 2021, *ApJ*, 908, 172
- Suzuki, T. K., & Inutsuka, S.-i. 2005, *Astrophys. J. Lett.*, 632, L49
- Szente, J., Landi, E., & van der Holst, B. 2022, *ApJ*, 926, 35
- . 2023, *ApJS*, 269, 37

- Tóth, G., Sokolov, I. V., Gombosi, T. I., et al. 2005, *Journal of Geophysical Research (Space Physics)*, 110, 12226
- Tóth, G., van der Holst, B., Sokolov, I. V., et al. 2012, *Journal of Computational Physics*, 231, 870
- Tu, C.-Y., & Marsch, E. 1997, *Solar Phys.*, 171, 363
- Ulrich, R. K., Evans, S., Boyden, J. E., & Webster, L. 2002, *ApJS*, 139, 259
- Uppendran, V., Cheung, M. C. M., Hanasoge, S., & Krishnamurthi, G. 2020, *Space Weather*, 18, e02478
- Upton, L., & Hathaway, D. H. 2014a, *ApJ*, 792, 142
- . 2014b, *ApJ*, 780, 5
- Usmanov, A. V., Goldstein, M. L., Besser, B. P., & Fritzer, J. M. 2000, *J. Geophys. Res.*, 105, 12,675
- Usmanov, A. V., Matthaeus, W. H., Goldstein, M. L., & Chhiber, R. 2018, *ApJ*, 865, 25
- van der Holst, B., Manchester, W. B., I., Klein, K. G., & Kasper, J. C. 2019, *ApJL*, 872, L18
- van der Holst, B., Sokolov, I. V., Meng, X., et al. 2014, *ApJ*, 782, 81
- van der Holst, B., Huang, J., Sachdeva, N., et al. 2022, *ApJ*, 925, 146
- Vásquez, A. M., van Ballegoijen, A. A., & Raymond, J. C. 2003, *ApJ*, 598, 1361
- Verdini, A., Velli, M., Matthaeus, W. H., Oughton, S., & Dmitruk, P. 2010, *Astrophys. J. Lett.*, 708, L116
- Wang, Y. M., & Sheeley, N. R., J. 1990, *ApJ*, 355, 726
- . 1992, *ApJ*, 392, 310
- Yamauchi, Y., Moore, R. L., Suess, S. T., Wang, H., & Sakurai, T. 2004, in *Astronomical Society of the Pacific Conference Series*, Vol. 325, *The Solar-B Mission and the Forefront of Solar Physics*, ed. T. Sakurai & T. Sekii, 301